Hindawi Publishing Corporation
EURASIP Journal on Wireless Communications and Networking
Volume 2006, Article ID 19460, Pages 1–10
DOI 10.1155/WCN/2006/19460

Outage Analysis of Ultra-Wideband System in Lognormal Multipath Fading and Square-Shaped Cellular Configurations

Pekka Pirinen

Centre for Wireless Communications, University of Oulu, P.O. Box 4500, FI-90014, Finland

Received 1 September 2005; Revised 11 October 2005; Accepted 4 December 2005

Generic ultra-wideband (UWB) spread-spectrum system performance is evaluated in centralized and distributed spatial topologies comprising square-shaped indoor cells. Statistical distributions for link distances in single-cell and multicell configurations are derived. Cochannel-interference-induced outage probability is used as a performance measure. The probability of outage varies depending on the spatial distribution statistics of users (link distances), propagation characteristics, user activities, and receiver settings. Lognormal fading in each channel path is incorporated in the model, where power sums of multiple lognormal signal components are approximated by a Fenton-Wilkinson approach. Outage performance of different spatial configurations is outlined numerically. Numerical results show the strong dependence of outage probability on the link distance distributions, number of rake fingers, and path losses.

1. INTRODUCTION

Ultra-wideband technology [1] offers competitive solutions to high-rate short-range wireless communication purposes (e.g., home multimedia). Also, numerous practical applications for UWB are foreseen in the area of low-data-rate, low-cost, and low-complexity devices providing location and tracking capabilities [2] (e.g., wireless hospital applications). Inherent characteristics of UWB, such as high multipath resolution, low energy consumption, and peaceful coexistence with other radio-frequency systems, are also favourable to the emergence of UWB. Impulse-based UWB techniques can be seen as a special case of spread-spectrum (SS) techniques. Both can utilize direct-sequence (DS) and time-hopping (TH) modulation. Matched filters and rake receivers can be used for energy collection from the rich multipath channel. This paper assumes a generic SS-UWB system that requires some processing gain (integration of several pulses) to achieve the required quality of service.

System capacity can be measured by the number of users/devices/nodes that can be simultaneously supported within a predefined geographical area (cell). Capacity is therefore limited by the cochannel interference generated at the vicinity of the desired link receiver. Outage probability is a measure that links the aggregate interference to the quality of service. Channel amplitude is modelled to fluctuate according to a lognormal distribution. In the radio channel, several signals overlap and sum up, which implies calculation of power sums of multiple lognormal signals. Unfortunately, there is no known closed-form solution for this purpose. However, several approximate methods have been presented in the literature. Some of the most cited proposals are Fenton-Wilkinson (or just Wilkinson's) [3] and Schwartz-Yeh [4] approaches. Both schemes model the sum of two or greater number of lognormal random variables by another lognormal random variable. Later on, both approximations have been accommodated to include correlated random variables in, for example, [5, 6]. Recently, a new accurate and simple closed-form approximation to lognormal sum densities and cumulative distributions has been published [7]. It is based on low-order curve fitting on lognormal probability paper.

Due to the really wide bandwidth of UWB system, the signal fading averages out considerably and becomes much lower than in narrowband systems. It is stated in [6] that the accuracy of the Fenton-Wilkinson approximation is fairly good at the tail distributions (e.g., low outage probabilities) and with small standard deviations. For these reasons and simplicity, the Fenton-Wilkinson method is applied in this paper.

This paper completes and enhances the framework started in the prior publications [8, 9]. The main new contributions can be summarized as (1) the number of multipaths in the model is increased to a more realistic level in UWB

systems, (2) dual-slope path loss model is used, providing flexibility to model wide range of physical environments (line-of-sight/non-line-of-sight) and wall penetration losses, (3) spatial link distance distributions in square-shaped centralized and distributed topologies are derived, simulated, and illustrated, (4) multiple-cell configurations are incorporated in the evaluation, and (5) numerical results of the extended model are shown.

The rest of the paper is organized as follows. Section 2 describes propagation channel modelling, derivation of link distance probability statistics for different cell topologies, and impact of UWB pulse waveform timing inaccuracies at the receiver. A procedure for outage probability analysis is explained in Section 3. A set of numerical results is presented in Section 4. Finally, concluding remarks are given in Section 5.

2. SYSTEM DESCRIPTION

2.1. Multipath channel model

Saleh and Valenzuela [10] have proposed a multicluster, exponentially decaying statistical channel model for indoor multipath propagation. Although their model did not cover ultra-widebands, it has worked as a foundation for UWB channel modelling. As a result, modified Saleh-Valenzuela models for UWB wireless personal area networks are described in [11]. The UWB channel measurements analyzed in [11] indicate that a lognormal distribution fits better than a Rayleigh distribution for the multipath gain magnitudes. Lognormal fading model has been used, for example, in [12]. Nakagami distribution has also been reported to have high correlation with the measured data. Irrespective of the instantaneous short-term distribution, after some time averaging, the long-term distribution (shadowing) generally tends to be lognormal.

This paper concentrates on system-level studies, and thus a simplified version of the modified Saleh-Valenzuela UWB model is employed. Adopting a tapped-delay-line model, the channel impulse response can be written as

$$h(t) = \sum_{l=0}^{L-1} a_l \delta(t - \tau_l), \tag{1}$$

where l is the multipath delay index, L is the number of paths, a_l is the real-valued amplitude with lognormal absolute value, and τ_l is the path delay of multipath l. A generic exponentially decaying multipath intensity profile (MIP) is assumed. MIP can also be referred to as a power delay (or decay) profile (PDP). By using a notation $E[a_l^2] = \overline{\alpha_l}$, the mean power coefficients in a single-cluster MIP with regular known tap delays can be expressed as

$$\overline{\alpha_l} = \overline{\alpha_0} e^{-\lambda l}, \quad l, \lambda \geq 0, \tag{2}$$

where λ is the temporal (delay) decay parameter. The number of multipath components and the decay exponent may be varied according to the propagation environments. Total power of the L-path MIP is normalized to unity as

$$\sum_{l=0}^{L-1} \overline{\alpha_0} e^{-\lambda l} = 1. \tag{3}$$

2.2. Path loss model

Distance dependence of the average received power is taken into account in the path loss model. Dual-slope path model [13] is applied with the extension of potential losses due to walls. The basic model in dB scale becomes

$$\mathrm{PL}(d) = \begin{cases} 0, & 0 \leq d \leq 1, \\ c_0 \cdot \log_{10}(d), & 1 < d < d_{\mathrm{break}}, \\ c_1 + c_2 \cdot \log_{10}\left(\dfrac{d}{d_{\mathrm{break}}}\right) + L_w, & d \geq d_{\mathrm{break}}, \end{cases} \tag{4}$$

where distance d is in meters, and c_0, c_1, and c_2 are constants that depend on the propagation environment. Distance d_{break} denotes the breakpoint of the path loss slopes, and L_w accounts for the wall loss. Parameters c_0 and c_2 define the slopes at short and longer distances, respectively. It can be assumed that line-of-sight (LOS) conditions are valid at short distances, realized in $c_0 = 17$. It is likely that beyond the breakpoint non-line-of-sight (NLOS) is a valid assumption, leading to $c_2 = 35$ or even more. Constant $c_1 = c_0 \log_{10}(d_{\mathrm{break}})$ guarantees continuity of the model at the breakpoint in the absence of wall loss.

2.3. Single-square-cell network topologies and link distance distributions

Rectangular cell shape is a reasonable assumption for indoor cells (rooms). A square-shaped cell is a special case of rectangular shape and it has been chosen in this paper for further analysis. The methodology, however, can be extended to other regular or arbitrary cell shapes. Also, the analysis here is restricted to two-dimensional plane, which can easily be broadened to three-dimensional space. The size of the cell is dependent on the side of the square (denoted by a) that has been set to 5 m in the numerical examples. The desired and interfering users are assumed to be located within a square indoor cell (room) of the size 5 m × 5 m. Four different network scenarios are considered that can be divided to *centralized* and *distributed* setups. The centralized configuration is further divided into three alternatives where the fixed master node location is varied. The optimum coverage is obtained from the centralized master-slave topology where the master node is placed at the centre of the cell (*Scenario a*). Suboptimum placements of the master node include the middle of the square side (*Scenario b*) and the corner (*Scenario c*). It is assumed that the slave nodes are uniformly distributed over the cell area. In the distributed (ad hoc) topology (*Scenario d*), all nodes are equal (location uniformly distributed over the cell area) and form peer-to-peer connections. A sample illustration of these topologies is depicted in Figure 1. Solid lines correspond to the desired link and dashed lines represent three interfering links as an example.

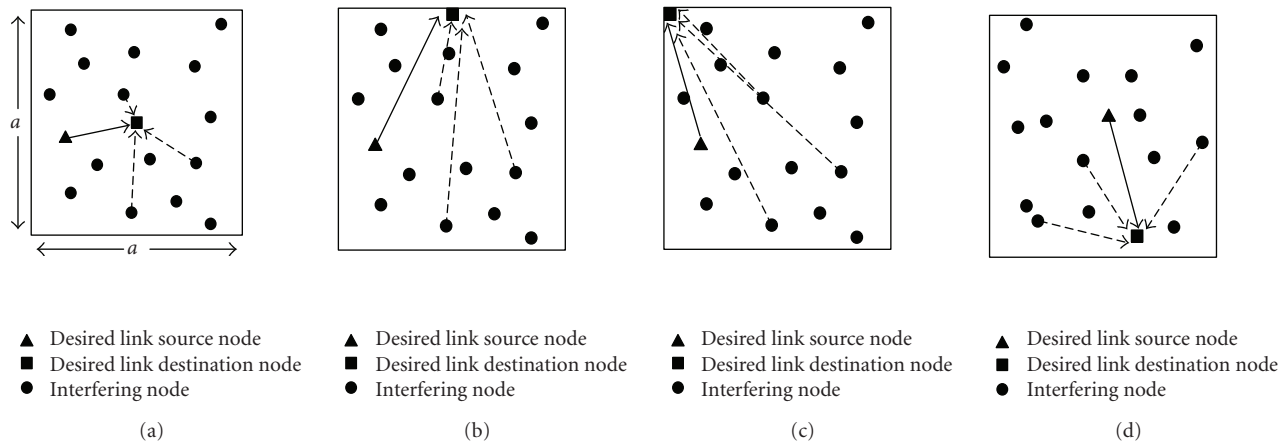

Figure 1: Four different spatial topologies within a square cell: (a) centralized topology ($d_{\max} = a/\sqrt{2}$); (b) centralized topology ($d_{\max} = \sqrt{5}a/2$); (c) centralized topology ($d_{\max} = \sqrt{2}a$); (d) centralized topology ($d_{\max} = \sqrt{2}a$).

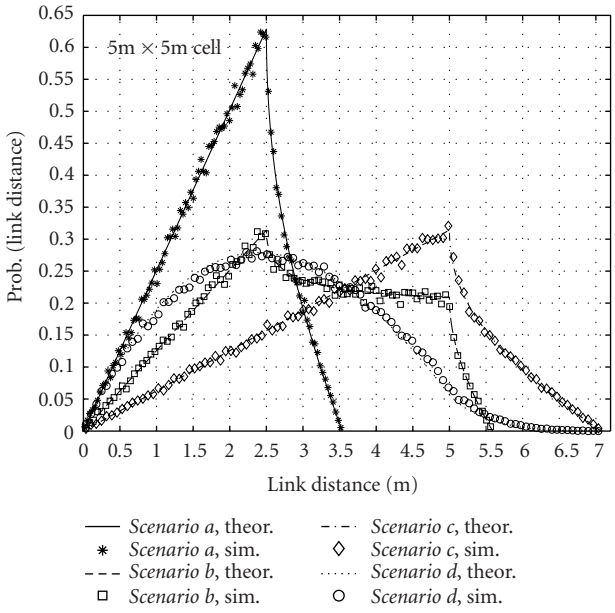

Figure 2: The link distance PDFs for different topologies within a square cell.

Distance-dependent PDFs can be easily solved in closed-form for certain regular cell topologies (e.g., [14–16] and references therein). Link distance PDFs for the topologies in Figure 1 are given in the appendix.

Probability density functions (A1)–(A4) are plotted in Figure 2 for $a = 5$ m. The validity of these equations has been cross-checked against PDFs extracted from the Monte Carlo simulations. In these simulations, 100000 randomly generated positions have been generated for the square-cell configurations of Figure 1. Then, probability density histograms with 100 evenly spaced distance bins have been created. It can be noted that the simulation results agree very well with the derived analytical expressions.

These PDFs correspond to the arc length at each link distance divided by the covered area. As an example in *Scenario a*, the PDF of link distance grows linearly in proportion to the circumference of the circle until the breakpoint $a/2$ that is the longest distance allowing a circle to fit inside the square cell. The largest link distances can only be realized when the slave nodes are near some of the corners. The corresponding probability mass (arc length) diminishes rapidly as a function of link length. The average link distances in *Scenario b* and *Scenario c* increase clearly in comparison to *Scenario a*. Drawbacks of these less favourable access point positions may be compensated with directional antennas.

The smooth shape of the distributed topology (*Scenario d*) distance PDF is evident because of the randomness in the generation of both ends of the link. The small tail of this distribution represents the longest link distances that can only be realized when both ends of the link are located at the vicinity of opposite corners.

Link distance cumulative distribution functions (CDFs) can be calculated by integrating PDFs over the whole range of possible link distances, for example,

$$P_{\mathrm{CDF}}(d_{\min} \le x \le d_{\max}) = \int_{d_{\min}}^{d_{\max}} p_{\mathrm{PDF}}(x)dx, \tag{5}$$

where $d_{\min} = 0$ in the case of (A1)–(A4).

Variations due to different spatial configurations can now be quantified by taking percentile segments of the link distance CDF. This method helps to avoid the heavy Monte Carlo simulations in the further analysis that needs link-distance-dependent path losses. Even if the link distance PDF and CDF are generated through simulation, the sufficient statistics can be extracted from only one simulation per scenario.

The path loss model (4) in decibels scales the mean values of each desired and interfering lognormal signal component by

$$m_{\mathrm{PL}} = m_0 - \mathrm{PL}\left(d^{x}_{\mathrm{scen}_{0j}}\right), \tag{6}$$

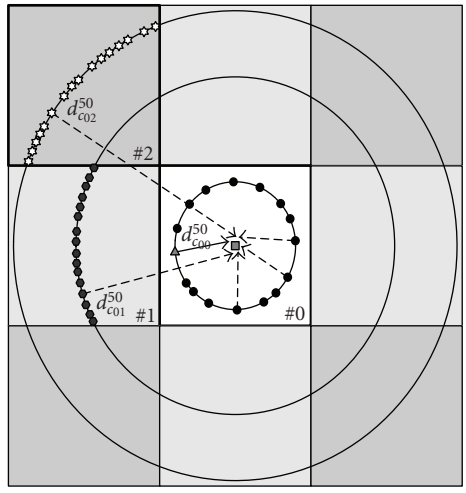

Figure 3: Centralized multiple-square-cell configuration.

where m_0 is the mean of the initial signal and $d^x_{\text{scen}_{0j}}$ is the link distance whose subscript specifies the spatial scenario (c for centralized and d for distributed topology), subsubscript indices 0 and $j \in [0, 1, 2, (1\&2)]$ localize the link ends with the respective cells and superscript the chosen link distance CDF percentile $x \in [10, 100]$ extracted from (5).

2.4. Extension to multiple-cell scenarios

Single-cell analysis can be extended to larger networks including multiple cells that will model the effect of intercell interference. In cellular systems, several surrounding layers may be required for a reliable estimate of the intercell interference statistics. However, due to the nature of the indoor environment and very low transmission powers assumed in this study, it is unlikely that significant cochannel interference would originate from very far. Signals will be even more isolated if there are thick walls between rooms. Based on these reasons and complexity restrictions, only one surrounding layer of square cells is modelled as potential origin for intercell interference. An example of the centralized multicell interference scenario is depicted in Figure 3.

The central cell in Figure 3, marked with #0, is the desired cell incorporating the link of interest and intracell interference links. Surrounding eight cells are divided into subgroups #1 (light grey) and #2 (dark grey), both including four square cells. Three circles with radii d_{c00}^{50}, d_{c01}^{50}, and d_{c02}^{50} represent median link distances between a destination node in cell #0 and source nodes in cells #0, #1, and #2, respectively. Due to geometrical symmetry, only these three cells are needed to fully characterize the link distance distributions of the scenario.

Intercell interference link distance PDFs can be calculated the same way as in the single-cell case. Restricting only to the centralized topology of Figure 3, the link distance PDF between the fixed central node in cell #0 and a uniformly distributed node location in cell #1 can be derived to be

$$p_{c_{01}}(d) = \begin{cases} \dfrac{2d}{a^2}\cos^{-1}\left(\dfrac{a}{2d}\right), & \dfrac{a}{2} \le d \le \dfrac{a}{\sqrt{2}}, \\ \dfrac{2d}{a^2}\sin^{-1}\left(\dfrac{a}{2d}\right), & \dfrac{a}{\sqrt{2}} < d \le \dfrac{3a}{2}, \\ \dfrac{2d}{a^2}\left[\sin^{-1}\left(\dfrac{a}{2d}\right) - \cos^{-1}\left(\dfrac{3a}{2d}\right)\right], & \dfrac{3a}{2} < d \le \dfrac{\sqrt{10}a}{2}. \end{cases} \tag{7}$$

Similarly, between the fixed central node in cell #0 and a random node position in cell #2, the link distance PDF becomes

$$p_{c_{02}}(d) = \begin{cases} \dfrac{\pi d}{2a^2} - \dfrac{2d}{a^2}\sin^{-1}\left(\dfrac{a}{2d}\right), & \dfrac{a}{\sqrt{2}} \le d \le \dfrac{\sqrt{10}a}{2}, \\ \dfrac{\pi d}{2a^2} - \dfrac{2d}{a^2}\cos^{-1}\left(\dfrac{3a}{2d}\right), & \dfrac{\sqrt{10}a}{2} < d \le \dfrac{3a}{\sqrt{2}}. \end{cases} \tag{8}$$

Finally, without division into subgroups, the link distance PDF between the central node in cell #0 and a randomly placed node within the combined area of cells #1 and #2 is formulated as

$$p_{c_{0(1\&2)}}(d) = \begin{cases} \dfrac{d}{a^2}\cos^{-1}\left(\dfrac{a}{2d}\right), & \dfrac{a}{2} \le d \le \dfrac{a}{\sqrt{2}}, \\ \dfrac{\pi d}{4a^2}, & \dfrac{a}{\sqrt{2}} < d \le \dfrac{3a}{2}, \\ \dfrac{\pi d}{4a^2} - \dfrac{d}{a^2}\cos^{-1}\left(\dfrac{3a}{2d}\right), & \dfrac{3a}{2} < d \le \dfrac{3a}{\sqrt{2}}. \end{cases} \tag{9}$$

These analytical PDF expressions are compared to the simulated distributions in Figure 4. Generally, a good agreement between theoretical and simulation results is shown. Only the middle segment of link 01 simulation has not been fully averaged out with the current sample size. It is worth noting that the shapes of link distance PDFs for links 01 and 02 differ drastically. However, it is easy to understand these differences by visually examining the cell geometry and the way the arc length changes along the distance. The link distance 0(1&2) PDF falls naturally between the other curves.

For the distributed topology, the intercell interference link distance statistics have not been derived. Instead, statistics based on simulations have been gathered. An example of simulated link distance CDFs according to (5) and topologies in Figures 1 and 3 is depicted in Figure 5. It can be seen that in general, the centralized scenario CDFs are steeper than the distributed scenario counterparts because of the more limited range in distances. As a result, the main differences between centralized and distributed topologies are in the low and high regions of CDFs. Around median link distances, there are only moderate deviations between them.

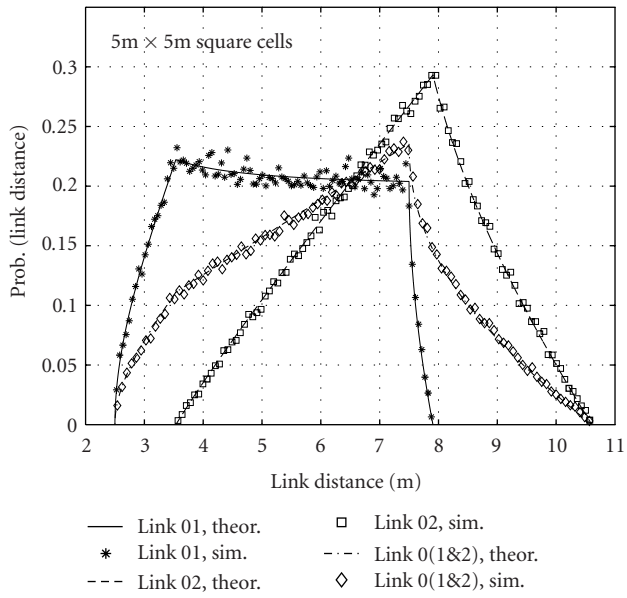

Figure 4: Intercell interference link distance PDFs for a centralized square-cell topology.

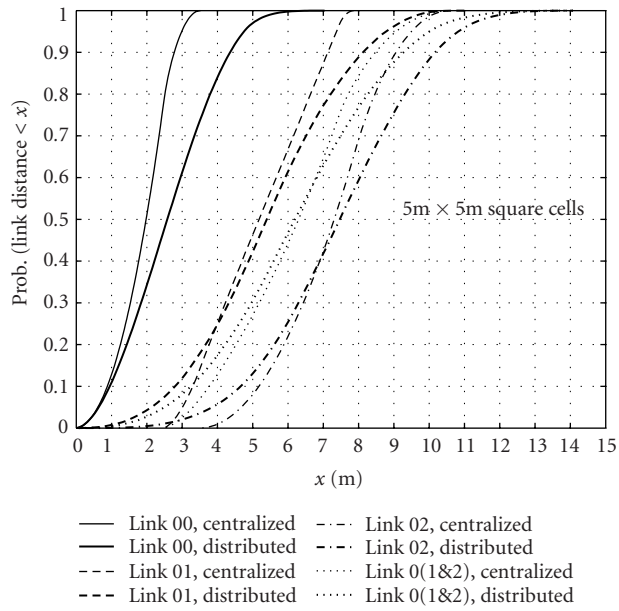

Figure 5: Simulated link distance CDFs for different square-cell topologies.

2.5. UWB pulse waveforms and impact of timing errors

A Gaussian monocycle is one of the most commonly assumed pulse waveforms in impulse-radio-(IR)-based UWB systems. The basic (zeroth derivative) zero-mean pulse can be defined as

$$w_{G_0}(t) = \frac{A}{\sqrt{2\pi}\sigma} \exp\left(-\frac{t^2}{2\sigma^2}\right), \tag{10}$$

where σ is the standard deviation of the Gaussian distribution and A is a generic amplitude scaling constant. According to studies in [17], the 5th-time derivative of (10) is the lowest-order waveform satisfying the Federal Communications Commission (FCC) indoor spectral emission mask requirements. Passing signal through an antenna can be approximated as an additional first-order differentiation of the pulse waveform [18]. Therefore, the generated waveform at the transmitter should be at least the 4th derivative of (10). The waveform seen at the receiver antenna output would then be the 6th derivative of (10), yielding

$$w_{G_6}(t) = A\left(\frac{t^6/\sigma^6 - 15t^4/\sigma^4 + 45t^2/\sigma^2 - 15}{\sqrt{2\pi}\sigma^7}\right) \exp\left(-\frac{t^2}{2\sigma^2}\right). \tag{11}$$

To ensure that most of the pulse energy will be captured, the duration of the pulse is set to be $T_p = 10\sigma$. The impact of timing errors (delay estimation, jitter) of the pulse waveforms in each receiver rake finger will be included by the following equations [8]:

$$\overline{\alpha_l}(\varepsilon) = R^2(\varepsilon)\overline{\alpha_l}, \tag{12}$$

$$\sigma_l^2(\varepsilon) = \sigma_l^2 + \left(1 - R^2(\varepsilon)\right)\frac{\overline{\alpha_0}}{\overline{\alpha_l}}, \tag{13}$$

where $R^2(\varepsilon)$ is the squared correlation function of the pulse waveform (11) with the normalized timing error $\varepsilon = t/T_p$. Variance in (13) depends on the severity of shadowing σ_l^2 per path, pulse autocorrelation, and power ratio of multipath components. Error variance, that is, the latter term in (13), is assumed to be inversely proportional to the delay tracking loop signal-to-noise ratio.

3. OUTAGE PROBABILITY ANALYSIS

User capacity can be defined as the maximum number of admissible active cochannel interferers satisfying a predefined outage criterion. The conditional outage probability is expressed as

$$P_{\text{out}}(I \mid n, m, L, L_0) = P\left(\frac{S}{I} = \frac{S(L_0)}{\left[I_{\text{INTRA}}(n) + I_{\text{INTER}}(m)\right]I_{\text{MPI}}(L) + I_{\text{IPI}}\left(L_0(L-1)\right)} < \left(\frac{S}{I}\right)_{\text{tar}}\right), \tag{14}$$

where S/I is the signal-to-interference power ratio, $S(L_0)$ is the desired signal power combined by L_0 rake fingers, and $(S/I)_{\text{tar}}$ is the target link quality requirement. Cochannel interference sources are n active multiaccess users in the desired cell (intracell interference I_{INTRA}) and m users in neighbouring cells (intercell interference I_{INTER}), all these signals spread over multiple propagation paths (I_{MPI}). Interpaths of the desired user link (I_{IPI}) also produce interference that depends on the number of rake fingers deployed at the receiver. The system is assumed to be interference limited, that is, the thermal noise power is significantly lower than the cochannel interference power, and therefore omitted.

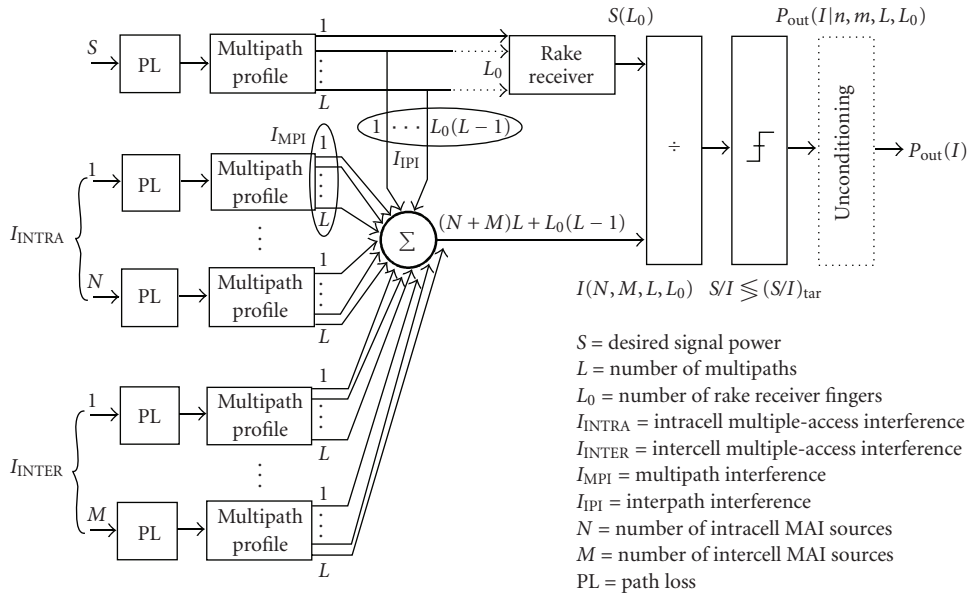

Figure 6: Block diagram for signal-to-interference ratio and outage calculation.

Overall outage probability can be calculated by unconditioning (14) with the probability density function of n intracell interferers being active while keeping m, L, and L_0 fixed. Therefore, we can write

$$P_{\text{out}}(I) = \sum_{n=1}^{N} P_{\text{out}}(I \mid n) P_n(n), \tag{15}$$

where $P_{\text{out}}(I)$ denotes the outage probability that accounts for the interference probability density function of n active interferers $P_n(n)$. Assuming a binomial PDF for $P_n(n)$, it becomes

$$P_n(n) = \binom{N}{n} P_{\text{act}}^n \left(1 - P_{\text{act}}\right)^{N-n}, \tag{16}$$

where N is the maximum number of cochannel interferers and P_{act} is the activity factor of these interfering sources.

In any spread-spectrum system, there is a simple relation between channel signal-to-interference ratio and baseband bit energy-to-interference power spectral density. It can be formulated as

$$\frac{S}{I} = \frac{R_b E_b}{R_c I_0} = \frac{E_b/I_0}{PG}, \tag{17}$$

where $PG = R_c/R_b$ is the processing gain, that is, a ratio of the spread chip rate R_c (UWB signal bandwidth) and the bit rate R_b. Required E_b/I_0 values depend on various link-level parameters (e.g., data rate, modulation, bit error rate), and can be obtained via simulations. However, this paper simply focuses on the generic S/I target.

Figure 6 shows a block diagram for the S/I and outage evaluation procedure. The desired signal with transmitted power S travels along the upper branch. It will be attenuated by the distance-dependent path loss (block PL), and finally the strongest L_0 fingers are combined in the selective rake receiver ($L_0 \leq L$). The lower branches represent interference that is a sum of N desired cell multiple-access signals through L-path channels, M neighbouring cell multiple-access signals through L-path channels, and interpath interference of the desired user through $L_0(L-1)$ paths. The last block in the chain with the label unconditioning refers to calculus shown in (15).

Equation (14) depends on the mean and variance of the lognormal sum distribution. By further conditioning the outage probability on n intracell interferers, m intercell interferers, and L_0 rake fingers, a slightly modified expression from [6] can be derived as

$$P_{\text{out}}\left(I \mid n, m, L, L_0\right) = 1 - Q\left(\frac{\ln(S/I)_{\text{tar}} - m_d(L_0) + m_z(n, m, L, L_0)}{\sqrt{\sigma_d^2(L_0) + \sigma_z^2(n, m, L, L_0) - 2 r_{dz} \sigma_d(L_0) \sigma_z(n, m, L, L_0)}}\right), \tag{18}$$

where $Q(x) = (1/\sqrt{2\pi}) \int_x^\infty e^{-u^2/2} du$ is a zero-mean, unit variance Gaussian complementary distribution function, u is a dummy integration variable, $m_d(L_0)$ is the area-mean desired signal power at the output of L_0-finger rake, $m_z(n, m, L, L_0)$ is the area-mean total cochannel interference power, $\sigma_d(L_0)$ is the standard deviation of the desired signal at the output of L_0-finger rake, $\sigma_z(n, m, L, L_0)$ is the standard deviation of the total cochannel interference, and r_{dz} is the correlation coefficient of the desired signal and joint interference.

Overall cochannel interference mean and standard deviation in (18) can be calculated through successive use of the lognormal sum approximation. Partial contributions in the final distribution can be divided into intracell, intercell, and

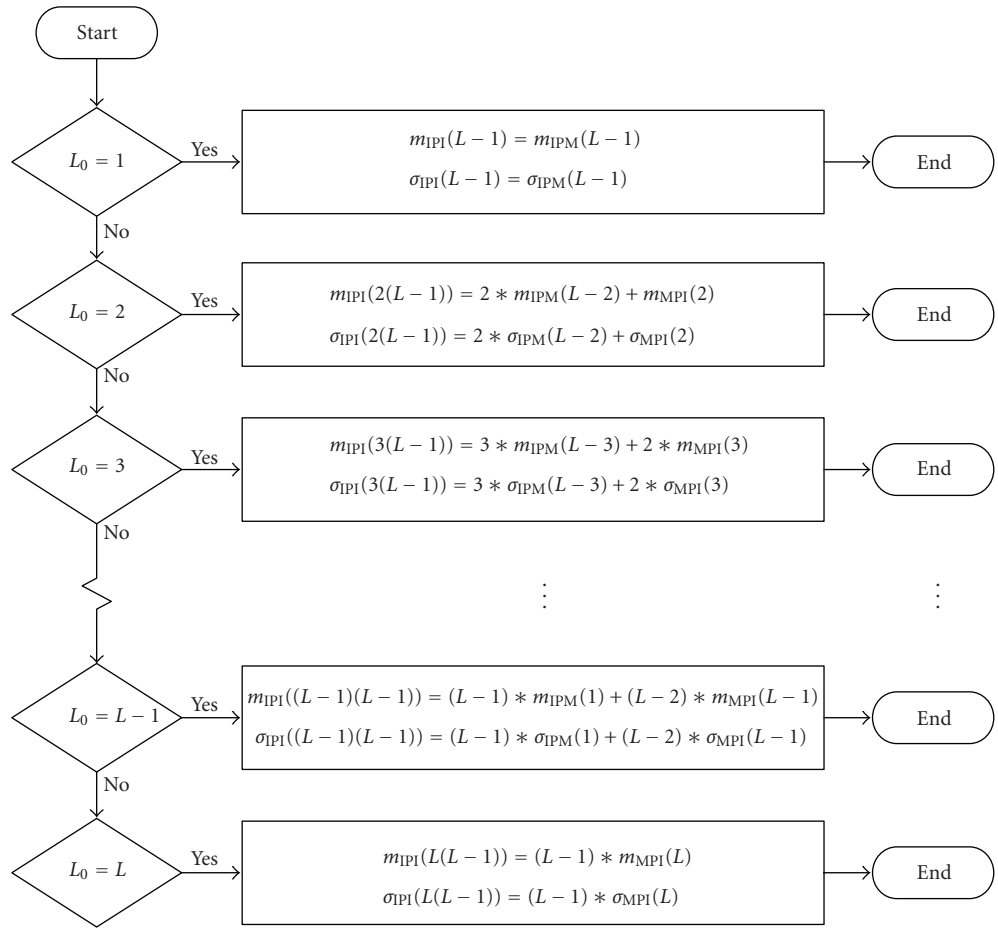

Figure 7: Flowchart of the interpath interference statistics calculation.

desired link interpath interference components as

$$\begin{aligned} m_z(n,m,L,L_0) &= \sum_n m_{\mathrm{INTRA}}(L) + \sum_m m_{\mathrm{INTER}}(L) + m_{\mathrm{IPI}}\big(L_0(L-1)\big), \\ \sigma_z(n,m,L,L_0) &= \sum_n \sigma_{\mathrm{INTRA}}(L) + \sum_m \sigma_{\mathrm{INTER}}(L) + \sigma_{\mathrm{IPI}}\big(L_0(L-1)\big). \end{aligned} \tag{19}$$

Aggregate interference is calculated with respect to indices $n = 1,\ldots,N$, and $m = 1,\ldots,M$, that is, the number of active intra- and intercell interference sources. All multipath profiles include L independent components. The number of interpath interference components depends on the diversity order L_0 in the rake combiner in addition to the number of multipaths. Figure 7 represents a flowchart on the mean and standard deviation of the interpath interference accumulation (last summands in (19)), depending on the number of rake fingers.

Lognormal sum statistics m_{MPI} and σ_{MPI} are calculated based on the MIP presented in (2). If the power coefficients of the exponential multipath profile are collected into vector $\vec{\boldsymbol{\alpha}} = [\overline{\alpha_0}\ \ \overline{\alpha_1}\ \ \cdots\ \ \overline{\alpha_{L-2}}\ \ \overline{\alpha_{L-1}}]$, the argument tells how many strongest paths are summed up. For statistics m_{IPM} and σ_{IPM}, the process is otherwise similar with the exception that the path vector is reversed as $\overleftarrow{\boldsymbol{\alpha}} = [\overline{\alpha_{L-1}}\ \ \overline{\alpha_{L-2}}\ \ \cdots\ \ \overline{\alpha_1}\ \ \overline{\alpha_0}]$. Now the argument refers to the number of weakest paths contributing to the sum.

4. NUMERICAL EXAMPLES

A generic spread-spectrum UWB system is assumed, targeted for $S/I = -17$ dB. All signal components are uncorrelated. The partial rake receiver of the desired user combines L_0 strongest paths as noncoherent lognormal power sum. Path loss breakpoints and wall losses are set for the desired cell links as $d_{\mathrm{break}} > d_{d_{00}}^{100}$ ensuring that $L_w = 0$ dB. For the interference links from cells of type #1, the corresponding parameters are $d_{\mathrm{break}} = d_{d_{01}}^{10}$ and $L_w = 10$ dB, and for the category #2 $d_{\mathrm{break}} = d_{d_{02}}^{10}$ and $L_w = 20$ dB, respectively. Table 1 includes more parameters and variables chosen for the forthcoming numerical results. Bold-faced numbers are nominal values that may be fixed or varied in the illustrations.

Figures 8 and 9 demonstrate the dependence of conditional outage probability on the number of rake fingers at the receiver. In Figure 8, the centralized single-cell topology is

Table 1: Key parameters in the numerical examples.

Number of multipaths L	**24**
Number of rake fingers L_0	$1,\ldots,\mathbf{6},\ldots,24$
MIP decay parameter λ	$\mathbf{1/4.3 \approx 0.23256}$
$m_d(1) = m_z(1)$ (dB)	$\mathbf{-6.8135}$
$\sigma_d(1) = \sigma_z(1)$ (dB)	**3.4**
Link distance CDF (%)	$10,\ldots,\mathbf{50},\ldots,100$
Interferer activity factor P_{act}	$0.1,\ldots,\mathbf{0.5},\ldots,1$
Path loss constants c_0, c_2	**17**, **35**
Max. number of intracell interferers N	**23**
Max. number of intercell interferers M	$\mathbf{8 \times 24}$
Timing error $\varepsilon[t/T_p]$	$\mathbf{0},\ldots,0.045$

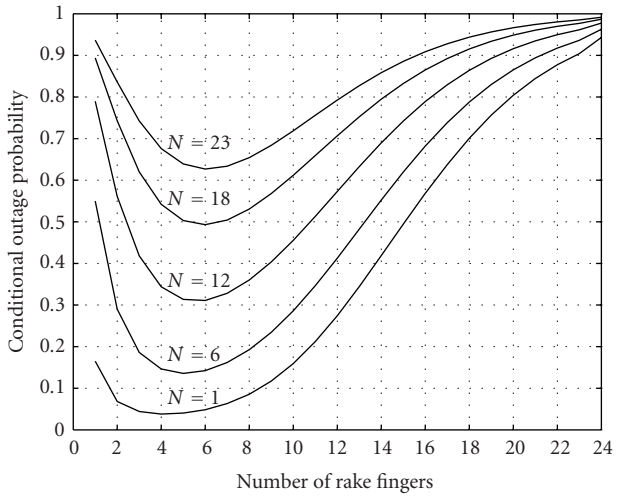

Figure 8: Number of rake fingers versus conditional outage probability in a centralized single-cell configuration.

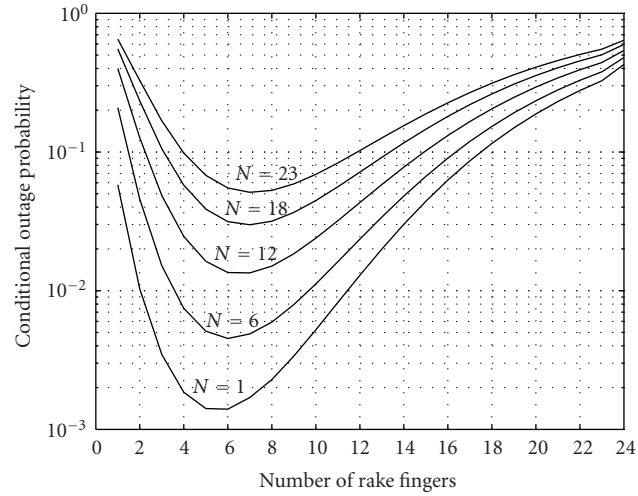

Figure 9: Number of rake fingers versus conditional outage probability in a distributed multicell configuration.

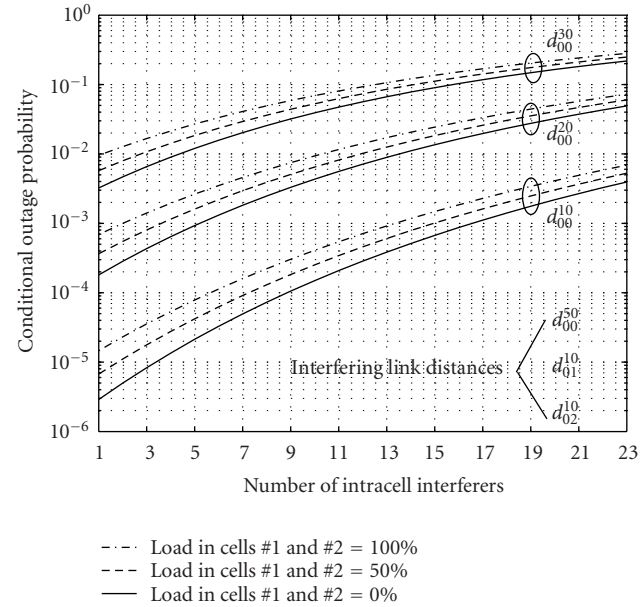

Figure 10: Impact of the intercell interference in a centralized multicell scenario.

chosen (see Figure 1(a)). Desired link and intracell interference distances are set to $d_{c_{00}}^{50} \approx 1.99$ m. It can be seen that the optimum number of fingers barely depends on the intracell load, and varies between 4 and 6. Figure 9 shows another setting with a distributed multicell configuration. In this case, the desired link distance follows $d_{d_{00}}^{20} \approx 1.44$ m, intracell interference $d_{d_{00}}^{50} \approx 2.56$ m, intercell interference $d_{d_{01}}^{50} \approx 5.41$ m, and $d_{d_{02}}^{50} \approx 7.39$ m. The impact of all 192 intercell interference nodes is accounted for. The optimal selection of rake fingers is now between 5 and 7. These quite different network configurations and outage levels produce very similar outcome. As a conclusion of both cases, we can state that only moderate complexity (approximately 6 rake fingers) is required for optimal performance even in the rich multipath channel.

Figure 10 depicts the impact of intercell load to the conditional outage probability at short desired link distances $d_{c_{00}}^{30}$ ($\approx$ 1.55 m), $d_{c_{00}}^{20}$ ($\approx$ 1.26 m), and $d_{c_{00}}^{10}$ ($\approx$ 0.89 m), while the intracell interferer link distances are maintained at $d_{c_{00}}^{50}$ ($\approx$ 1.99 m). On the other hand, the effect of intercell interference is emphasized by locating cell #1 and cell #2 nodes near the edge of the centre cell at link distances $d_{c_{01}}^{10}$ ($\approx$ 3.33 m) and $d_{c_{02}}^{10}$ ($\approx$ 5.19 m). We can note that the intracell interference still dominates the performance, and aggregate intercell interference can only have marginal effect on the desired link conditional outage probability. Naturally, the geometry of the link of interest plays a key role in the observed outage level.

Figure 11 shows how the outage probability behaves as a function of the desired link distance CDF percentile and intracell interference activity factor. Six rake fingers are deployed due to the previously shown results. The load in cell

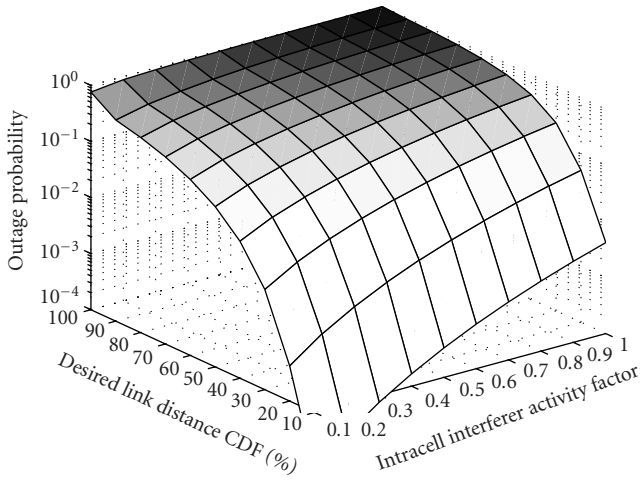

Figure 11: Outage probability as a function of intracell interference activity and desired link distance percentile in a centralized multicell scenario.

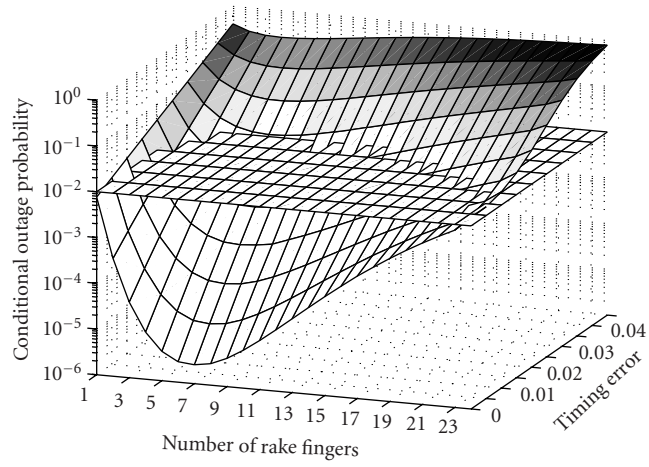

Figure 12: Effect of timing error (Gaussian 6th derivative) in a distributed multicell scenario.

types #1 and #2 is set to 50% (8×12 intercell interferers active). Intracell interference link distances are set to $d_{c_{00}}^{50} \approx 1.99$ m. Intercell interference link distances are $d_{c_{01}}^{50} \approx 5.21$ m and $d_{c_{02}}^{50} \approx 7.33$ m, respectively. As expected, the outage probability increases smoothly as a function of both variables.

Figure 12 illustrates the impact of normalized timing errors in the receiver correlation of the 6th-derivate Gaussian pulse (11) according to delay estimation errors extracted from (12) and (13). The desired link distance is $d_{d_{00}}^{10} \approx 0.97$ m. The interfering link distances are $d_{d_{00}}^{50} \approx 2.56$ m, $d_{d_{01}}^{50} \approx 5.41$ m, and $d_{d_{02}}^{50} \approx 7.39$ m. Intracell interference is limited to $N = 1$, and intercell load is set to 50% ($M = 8 \times 12$). A reference plane is plotted at the conditional outage probability of 10^{-2}. Clearly, the high-order derivation reduces robustness against timing errors. Also, in the presence of timing errors, the optimal number of rake fingers tends to decrease (gradually from 7 to 4). A timing error of only $0.035T_p$ is enough to exceed the reference level at any number of rake fingers.

5. CONCLUSIONS

Analytical evaluations of the cochannel interference limited outage probabilities were conducted. Square-shaped cell topologies with either centralized or distributed scenarios were assumed, and link distance probability density functions for these cell configurations were derived and simulated. Lognormal multipath propagation parameters, aggregate intra- and intercell multiuser interference, rake receiver finger allocation, and user activity were taken into account in the calculations. Numerical results show that a moderate number of rake fingers is enough even in dense multipath channel. Optimal number of rake fingers is rather insensitive to parameter variations. Relative distances and path losses of the desired link and interfering links have a strong impact on the detected outage probability. Intracell interference has much stronger impact on outage performance than intercell interference. Sensitivity to UWB pulse waveform timing uncertainty is evident for the 6th-derivate Gaussian pulse at the receiver output (5th-derivate waveform in the radio channel). Differences between centralized and distributed topology link distance PDFs are obvious but much less notable in outage probability.

APPENDIX

PDF for the link distance in the centralized *Scenario a* of Figure 1 becomes [9]

$$p_{c_a}(d) = \begin{cases} \dfrac{2\pi d}{a^2}, & 0 \le d \le \dfrac{a}{2}, \\ \dfrac{2\pi d}{a^2} - \dfrac{8d}{a^2}\cos^{-1}\left(\dfrac{a}{2d}\right), & \dfrac{a}{2} < d \le \dfrac{a}{\sqrt{2}}. \end{cases} \tag{A.1}$$

PDF for the link distance in *Scenario b* is slightly more complicated because it is composed of three segments. After some geometry sketches and trigonometric calculations, the following formula was derived:

$$p_{c_b}(d) \begin{cases} \dfrac{\pi d}{a^2}, & 0 \le d \le \dfrac{a}{2}, \\ \dfrac{\pi d}{a^2} - \dfrac{2d}{a^2}\cos^{-1}\left(\dfrac{a}{2d}\right), & \dfrac{a}{2} < d \le a, \\ \dfrac{2d}{a^2}\left[\sin^{-1}\left(\dfrac{a}{d}\right) - \cos^{-1}\left(\dfrac{a}{2d}\right)\right], & a < d \le \dfrac{\sqrt{5}a}{2}. \end{cases} \tag{A.2}$$

In *Scenario c*, the PDF resembles a lot the one derived for *Scenario a* and it becomes

$$p_{c_c}(d) = \begin{cases} \dfrac{\pi d}{2a^2}, & 0 \le d \le a, \\ \dfrac{\pi d}{2a^2} - \dfrac{2d}{a^2}\cos^{-1}\left(\dfrac{a}{d}\right), & a < d \le \sqrt{2}a. \end{cases} \tag{A.3}$$

For the distributed peer-to-peer topology in *Scenario d*, the corresponding link distance PDF has been used in the random waypoint mobility model [15] and it is written as [9]

$$p_{d_d}(d)\begin{cases}\dfrac{2d}{a^2}\left(\dfrac{d^2}{a^2}-\dfrac{4d}{a}+\pi\right), & 0\le d\le a,\\[2ex] \dfrac{4d}{a^2}\left[\sin^{-1}\left(\dfrac{a}{d}\right)-\cos^{-1}\left(\dfrac{a}{d}\right)-1\right] & \\ \quad+\dfrac{8d}{a^3}\sqrt{d^2-a^2}-\dfrac{2d^3}{a^4}, & a<d\le\sqrt{2}a.\end{cases} \tag{A.4}$$

ACKNOWLEDGMENTS

This study has been funded in part by the Finnish Funding Agency for Technology and Innovation of Finland (Tekes), Elektrobit, the Finnish Defence Forces through CUBS Project, and the Academy of Finland through CAFU Project (no. 104783). The author would like to thank the sponsors for their support. Professor Jari Iinatti is also gratefully acknowledged for his valuable comments.

REFERENCES

[1] S. Roy, J. R. Foerster, V. S. Somayazulu, and D. G. Leeper, "Ultrawideband radio design: the promise of high-speed, short-range wireless connectivity," *Proceedings of the IEEE*, vol. 92, no. 2, pp. 295–311, 2004.

[2] "PULSERS Integrated Project (IST 506897)," http://www.pulsers.net.

[3] L. F. Fenton, "The sum of log-normal probability distributions in scatter transmission systems," *IEEE Transactions on Communications*, vol. 8, no. 1, pp. 57–67, 1960.

[4] S. C. Schwartz and Y. S. Yeh, "On the distribution function and moments of power sums with log-normal components," *Bell Systems Technical Journal*, vol. 61, no. 7, pp. 1441–1462, 1982.

[5] C.-L. Ho, "Calculating the mean and variance of power sums with two log-normal components," *IEEE Transactions on Vehicular Technology*, vol. 44, no. 4, pp. 756–762, 1995.

[6] A. A. Abu-Dayya and N. C. Beaulieu, "Outage probabilities in the presence of correlated lognormal interferers," *IEEE Transactions on Vehicular Technology*, vol. 43, no. 1, pp. 164–173, 1994.

[7] N. C. Beaulieu and F. Rajwani, "Highly accurate simple closed-form approximations to lognormal sum distributions and densities," *IEEE Communications Letters*, vol. 8, no. 12, pp. 709–711, 2004.

[8] P. Pirinen, "Outage evaluation of ultra wideband spread spectrum system with RAKE combining in lognormal fading multipath channels," in *Proceedings of IEEE 15th International Symposium on Personal, Indoor and Mobile Radio Communications (PIMRC '04)*, vol. 4, pp. 2446–2450, Barcelona, Spain, September 2004.

[9] P. Pirinen, "Ultra wideband system outage studies in a square cell with partial rake receiver and lognormal fading," in *Proceedings of IEEE International Conference on Ultra-Wideband (ICU '05)*, pp. 230–235, Zurich, Switzerland, September 2005.

[10] A. A. M. Saleh and R. A. Valenzuela, "A statistical model for indoor multipath propagation," *IEEE Journal on Selected Areas in Communications*, vol. 5, no. 2, pp. 128–137, 1987.

[11] A. F. Molisch, J. R. Foerster, and M. Pendergrass, "Channel models for ultrawideband personal area networks," *IEEE Wireless Communications*, vol. 10, no. 6, pp. 14–21, 2003.

[12] J. Zhang, R. A. Kennedy, and T. D. Abhayapala, "Performance of RAKE reception for ultra wideband signals in a lognormal-fading channel," in *Proceedings of International Workshop on Ultra Wideband Systems (IWUWBS '03)*, Oulu, Finland, June 2003.

[13] R. Giuliano and F. Mazzenga, "On the coexistence of power-controlled ultrawide-band systems with UMTS, GPS, DCS1800, and fixed wireless systems," *IEEE Transactions on Vehicular Technology*, vol. 54, no. 1, pp. 62–81, 2005.

[14] S. W. Oh and K. H. Li, "Effects of simplified cellular configuration on performance of Rayleigh-faded forward-link CDMA system with power control," *Electronics Letters*, vol. 34, no. 23, pp. 2201–2202, 1998.

[15] C. Bettstetter, H. Hartenstein, and X. Pérez-Costa, "Stochastic properties of the random waypoint mobility model," *Wireless Networks*, vol. 10, no. 5, pp. 555–567, 2004, Special issue on modeling and analysis of mobile networks.

[16] E. W. Weisstein, "Square line picking," from MathWorld—A Wolfram Web Resource, http://mathworld.wolfram.com/SquareLinePicking.html.

[17] H. Sheng, P. Orlik, A. M. Haimovich, L. J. Cimini Jr., and J. Zhang, "On the spectral and power requirements for ultra-wideband transmission," in *Proceedings of IEEE International Conference on Communications (ICC '03)*, vol. 1, pp. 738–742, Anchorage, Alaska, USA, May 2003.

[18] F. Ramírez-Mireles and R. A. Scholtz, "Multiple-access with time hopping and block waveform PPM modulation," in *Proceedings of IEEE International Conference on Communications (ICC '98)*, vol. 2, pp. 775–779, Atlanta, Ga, USA, June 1998.

Pekka Pirinen received M.S. and Licentiate of Technology degrees in electrical engineering from the University of Oulu, Finland, in 1995 and 1998, respectively. Since 1994, he has been with the Telecommunication Laboratory and the Centre for Wireless Communications, University of Oulu, working as a Research Scientist in various European and national spread-spectrum, CDMA, and UWB research projects. He is also a Ph.D. student at the Telecommunication Laboratory. His research interests include multiaccess protocols, capacity evaluation, ultra-wideband communications, and wireless networks in general.